



Effect of support structures on Ti-6Al-4V overhang parts fabricated by powder bed fusion electron beam additive manufacturing

Xiaoqing Wang*, Kevin Chou

Department of Mechanical Engineering, The University of Alabama, Tuscaloosa, AL 35487, USA

ARTICLE INFO

Keywords:

Powder bed fusion electron beam additive manufacturing
Ti-6Al-4V
Microstructure
Texture
Support structure
Hardness

ABSTRACT

The effects of the two support structures, thin-wall tooth contact (TC) and solid-gap (SG), on the Ti-6Al-4V parts fabricated by powder bed fusion electron beam additive manufacturing were investigated. In the Y-plane of the overhang, equiaxed β' microstructure formed initially and gradually grew into a wider columnar structure with its width about 3 times of that in the solid section. Fine α/α' and β phases were identified within the β' grains, in which the content of α' increases from the bottom to the top of the part and α/α' phase presents strong textures of $\langle 0001 \rangle$ and $\langle 11\bar{2}0 \rangle$ parallel to the build-direction. In addition, more defects were observed in the overhang than the solid, especially at the interface between the solid and the overhang sections which also induced the stress concentration. Compressive residual stresses were revealed in the parts with some points showing minor tensile residual stresses. Compared to the SG part, the TC part had a lower Vickers hardness. The solid part under the SG part acted as a heat sink and enhanced heat dissipation during the manufacturing process, which affected the thermal gradient and improved the microstructures and mechanical properties in the overhang. The teeth in the TC part did limit the occurrence of the wrapping phenomenon. Taking advantages of the two designs, a new support design, SG support with teeth at the tip-end of overhang, is recommended.

1. Introduction

Powder bed fusion electron beam additive manufacturing (PBF-EBAM) (de Formanoir et al., 2016), also named as electron beam melting (EBM) (Arcam, 2018a), uses an electron beam to selectively melt a metallic powder-bed layer by layer to manufacture metal components. Compared with other additive manufacturing (AM) technologies, such as selective laser melting (SLM) (Wang and Chou, 2017a) and directed energy deposition (DED: powder-feed (Wang et al., 2016a) or wire-feed (Ding et al., 2017a)), EBM owns several unique advantages, such as high energy efficiency, fast scanning speed and less residual stress in the as-built parts (Lu et al., 2016). It has attracted ever-increasing interests from aerospace (Tan et al., 2015a), military and biomedical industries (Jamshidinia et al., 2014). Titanium alloys are finding expanding application in industries due to their high melting temperature, high strength to density ratio (Wang et al., 2015), and excellent properties and corrosion resistance (Facchini et al., 2009). These characteristics make them having comparative advantages over other competing metallic materials, such as magnesium alloys and steel (Hu et al., 2017). Ti-6Al-4V, as one of the most common titanium alloys, is the workhorse for many aerospace applications (airframes and turbine engines) and it accounts for more than 80% of the total US

market usage (Eylon and Seagle, 2001).

For the EBM-produced Ti-6Al-4V alloy, Al-Bermani et al. (2010) observed the columnar parent β grains in an as-built sample which was resulted from thermal characteristics of the EBM process, such as small melt pools and rapid cooling rates. Lu et al. (2016) found ultrafine lamellar α and β phases in the massive grains that transformed from prior β phases. Murr et al. (2009) measured the thickness of the fine α -lath in varied EBM samples and the value was around 1.4–2.1 μm , which was caused by the high cooling rates during the solidification. In addition, α' -martensitic platelets were observed in the samples (Gong et al., 2014) which had comparable mechanical properties with the counterpart from conventional methods (Toh et al., 2016). Formanoir et al. (de Formanoir et al., 2016) reported that horizontally built samples showed higher tensile properties which were also affected by the surface finish and the heat treatment. Vickers microhardness values were reported as varied from 345 to 350 HV (Hrabe and Quinn, 2013). The improvement in mechanical properties of EBM Ti-6Al-4V alloy was probably due to the fine α/β microstructure according to Hall-Petch relation, as mentioned by Gong et al. (2014). In summary, EBM-produced Ti-6Al-4V samples presented an ultrafine microstructure and tensile properties that are comparable with conventional counterparts.

Even though the EBM process has outstanding advantages in

* Corresponding author.

E-mail address: xwang127@crimson.ua.edu (X. Wang).

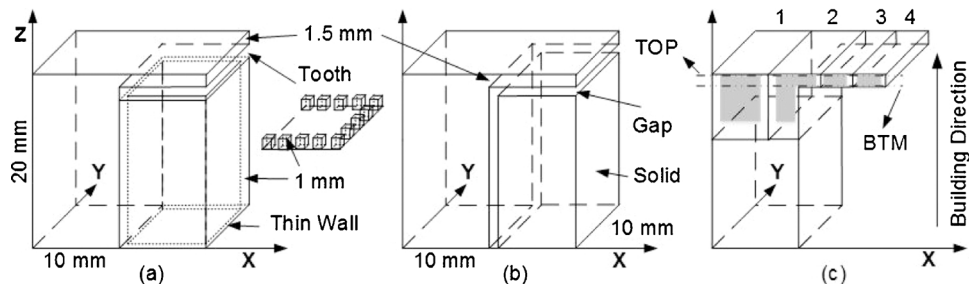


Fig. 1. Schematic of Ti-6Al-4V overhang parts: (a) thin wall tooth contact (TC) support design, (b) solid-gap (SG) support design, and (c) locations of the four samples (S1-4).

producing the Ti-6Al-4V alloy, it is still facing the challenges of the porosity (DebRoy et al., 2018), shape accuracy, and surface finish, and the control over microstructural morphology (Ding et al., 2016). Ideally, producing metal components using PBF-AM processes does not require support structures for overhangs as the overhangs can be supported by their surrounding raw powder (Zeng, 2015). However, the overhangs do need to be supported in practice, otherwise, defects can occur frequently, such as staircase effect, dross formation and warp (Calignano, 2014). When the energy beam scans the surface of the paved powder layer, the heat conduction rate is high at the solid-supported zones and becomes much lower at powder-supported regions, which is common to be observed in the manufacturing of parts with overhangs (Kruth et al., 2007). This results in a much higher absorbed energy input at the powder-supported zones, which can cause unintentional sintering of the powder particles beneath and consequently result in unsatisfactory downside skin finishes (Gan and Wong, 2016). The absorbed energy may also lead to a large melt pool to sink into the powder below due to the high gravity and capillary forces. Consequently, dross forms easily (Chivel and Smurov, 2011) and dimensional accuracy (Ding et al., 2017b) is not well controlled during fabrication of the overhangs. The rapid solidification during PBF-AM processes also induces thermal residual stress, which leads to the warping defect when the residual stress exceeds the strength of the material (Wang et al., 2016b). The support structure is an essential part as overhangs cannot always be eliminated through reorientation (Gan and Wong, 2016). Thomas and Bibb (2008) found that the laser powder-bed process was only capable of building unsupported overhangs inclined up to a maximum of 45° and below which support structures are required. The support structures function as anchors for initially floating objects (Jhabvala et al., 2012), dissipate melt pool heat, and prevent thermal warping of the parts (Vandenbroucke and Kruth, 2007).

However, the utilization of the support structure might raise substantially the material and energy consumption, as well as the manufacturing time and cost (Bobbio et al., 2017). To avoid or minimize support structures in the manufacturing process, support structures should be considered comprehensively during the whole product development process, from the phase of product design to the phase of final finishing. Multiple approaches have been developed to design and optimize the support structure, such as topology optimization (Langelaar, 2016). Using pure mathematical 3D implicit functions, Strano et al. (2013) proposed a method for the design and generation of the cellular support structures including graded supports. Poyraz et al. (2015) studied the effects of different parallel support structures on the density and the microstructure of the overhang geometry. Järvinen et al. (2014) compared the usability of the web and tube support structures and noticed that web supports have a better removability than the tube supports. After studying three types of support structures, Gan and Wong (2016) found three critical factors in manufacturing, which are the orientation of the parts during manufacturing, optimization of the support structure, and the quality of each printed layer. Using Taguchi L36 design and optimized supports, Calignano (2014) reported that it is possible to build non-assembly mechanism with overhang surfaces. In sum, most studies focus on the design and

optimization of the support structure and there are seldom studies available about the effect of the support structure on the microstructure and mechanical properties of the finishing parts.

With the aim to advance the adoption of the EBM technology, two Ti-6Al-4V parts with two different types of support structure were designed and manufactured. The two parts were used to investigate the effects of support structures on the microstructure and mechanical properties of the solid and the overhang in the final parts. The relationship between microstructure and mechanical properties was revealed, and the residual stress in the Y-plane was evaluated. Then, the features of the two different support structures were compared and discussed.

2. Experimental procedures

Two types of support structure were designed with the specific dimensions shown in Fig. 1. The thin wall tooth contact (TC) support is shown in Fig. 1a), in which only the top surface of the cuboid-tooth (1mm × 1 mm) are in intact with the overhang to supply the support and the remains of the region are filled with metal powder during the manufacturing process. The solid-gap (SG) support is shown in Fig. 1b, in which a support surface is put underneath the overhang. The gap between the support surface and the overhang was filled with unmelted metallic powder during manufacturing.

The two Ti-6Al-4V parts were manufactured by an Arcam S12 EBM system at Marshall Space Flight Center (Huntsville, AL). The Ti-6Al-4V powder, which has a particle size between 45 and 100 µm (Arcam, 2018b), was selectively melted layer by layer at the layer thickness of 70 µm. The default standard contour-hatching scanning strategy was employed and the beam scanning speed was 376 mm/s (Gong et al., 2014). Four samples (S1-S4) were cut along X-axis by the TechCut 4TM precision low speed saw with the location of them shown in Fig. 1c, in which S2 contains the transition zone from the solid to the overhang. They were prepared with the standard metallographic procedures for microstructure analysis. The final polished specimens were etched with the Kroll's Reagent and then examined using an optical microscope (OM) and a JOEL F7000 scanning electron microscope (SEM). Electron backscatter diffraction (EBSD) was also conducted using the JEOL 7000 SEM equipped with an EBSD camera to analysis the texture in the specimens with a scanning size of 500 µm by 500 µm and a step size of 1.5 µm.

To obtain the micro-hardness and estimate the residual stress in the samples, Vickers indentation test was carried out at the test load of 1 kgf and the loading time of 10 s. A pattern of 18 × 3 with the test points uniformly distributed on the surface of the samples was adopted. Under certain assumptions (Song et al., 2014; Wang and Chou, 2015), the equi-biaxial residual stress and the equi-biaxial residual strain follows the following relations.

$$H = C\sigma(\epsilon_{repr} + \epsilon_{res}) \quad (1)$$

$$c^2 = c_0^2 - 0.32\ln\left(1 + \frac{\sigma_{res}}{\sigma(\epsilon_{res})}\right) \quad (2)$$

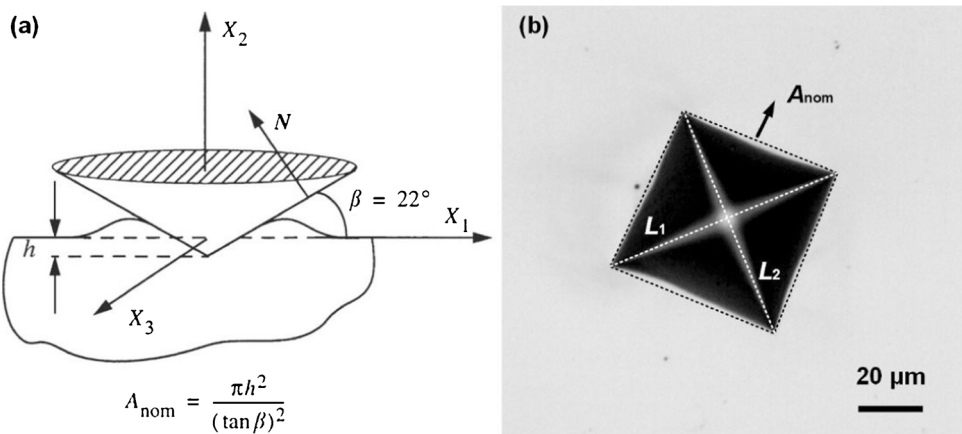
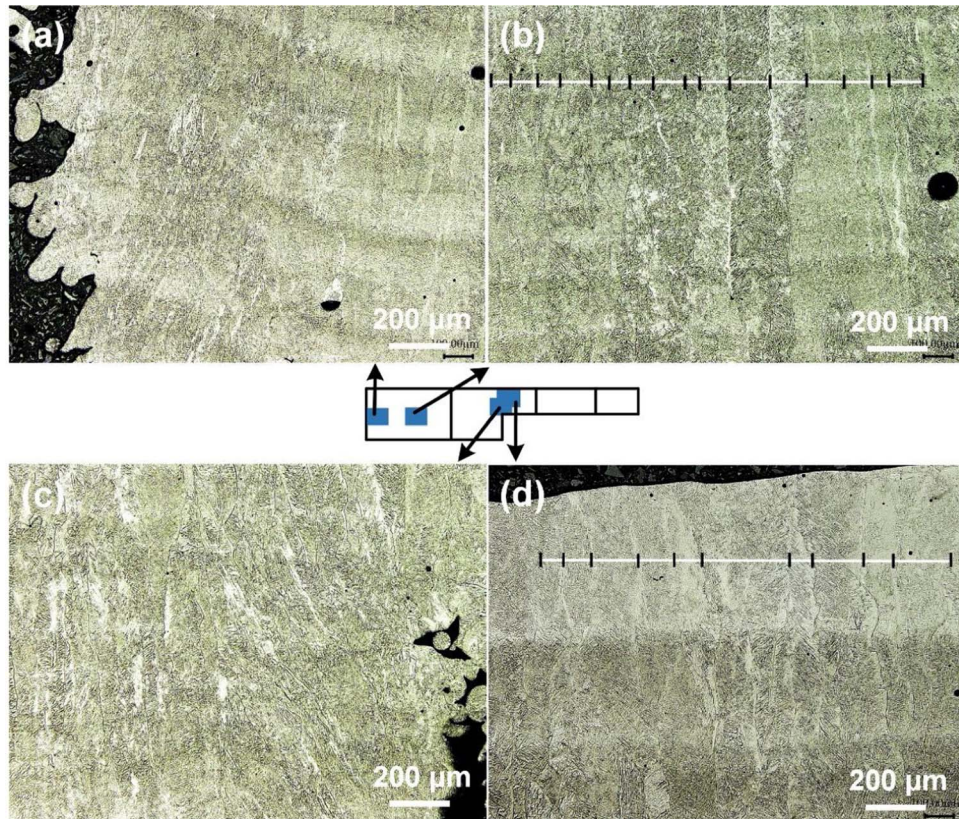


Fig. 2. Schematic of the Vickers indentation tests (Carlsson and Larsson, 2001) and (b) the nominal projected contact area A_{nom} .



where $H = P/A_{\text{real}}$ is the Vickers' hardness at the test point (P is the testing load, A_{real} is the projected real contact area), $C=3$, and $\sigma(\varepsilon_{\text{repr}} + \varepsilon_{\text{res}})$ is the flow stress at the representative strain and the residual strain. $\varepsilon_{\text{repr}} = 0.08$, is a value of the effective plastic strain and ε_{res} is the residual plastic strains. c^2 is the ratio of A_{real} to the nominal projected contact area A_{nom} and $c_0^2=1$ (Carlsson and Larsson, 2001). A_{nom} was calculated by the length of the two diagonals of the indentation, L_1 and L_2 , as shown in Fig. 2,

$$A_{\text{nom}} = \frac{1}{2} \left(\frac{(L_1 + L_2)}{2} \right)^2 \quad (3)$$

For EBM Ti-6Al-4V alloy, the stress-strain curve is obtained by Roy (2013). The power-law function below was fitted with the tensile results.

$$\sigma(\varepsilon_{\text{res}}) = \sigma_0 \varepsilon_{\text{res}}^n = 858 \varepsilon_{\text{res}}^{0.049} \quad (4)$$

Therefore, the residual stress in the EBM parts can be predicted by the equation below.

$$\sigma_{\text{res}} = 858 \left\{ \left[\frac{8 * P}{3 * 858 * (L_1 + L_2)^2} \right]^{\frac{1}{0.049}} - 0.08 \right\}^{0.049} * \left\{ e^{\left[\frac{1 - \frac{8 * A_{\text{real}}}{(L_1 + L_2)^2}}{0.32} \right]} - 1 \right\} \quad (5)$$

3. Results and discussions

3.1. Microstructure characteristics

The microstructure of the as-built EBM Ti-6Al-4V samples is shown in Figs. 3 and 4. Columnar prior β structures were revealed in S1, which

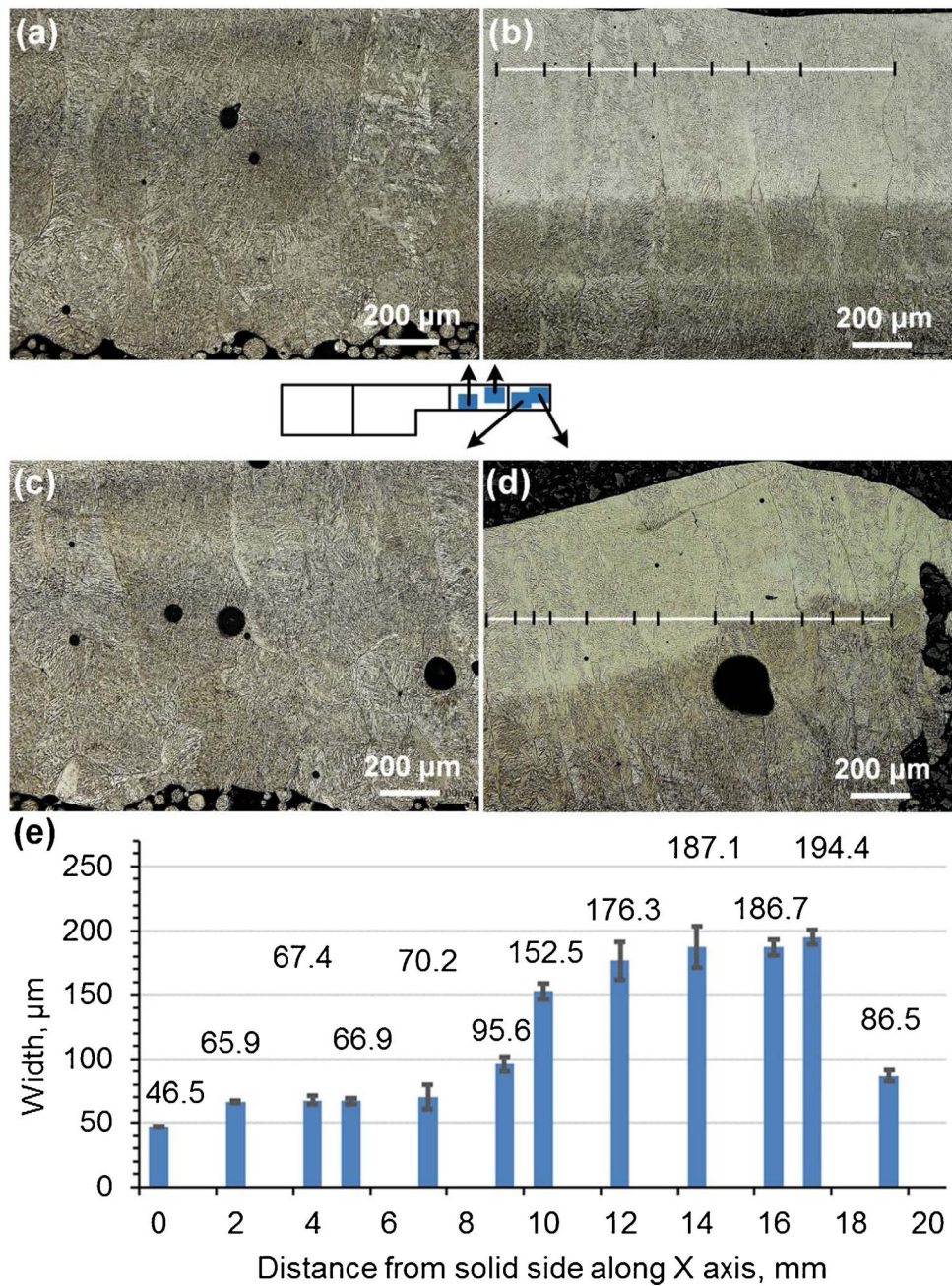


Fig. 4. EBM-fabricated Ti-6Al-4V TC sample: optical microstructure of (a, b) S3, and (c, d) S4, and (e) width of columnar structures changing along the X axis at the height close to the top end surface.

is a typical feature in metals subjected to rapid cooling processes, such as laser cladding (Ding and Kovacevic, 2016) and selective laser melting (Wang and Chou, 2017b). During the initial rapid solidification, the nucleation and growth of columnar prior β phase occurred when the temperature was above the β -transus temperature. They grew along the Z-axis (build direction) and across tens of layers in the specimen. This was significantly affected by the heat flux during solidification. The rapid heat loss via conduction from the melt pool to the stainless steel base plate was dominant at the initial stage of manufacturing process.

With the increase of the build height, the heat loss from the melt pool through the surrounding powder also occurred (Wang et al., 2016c). At the center position of the S1, the main direction of the prior β phase is the build direction (Z-axis), as shown in Fig. 3b. The prior β phases near the contour section grew at an oblique angle toward the

center of the specimen (Fig. 3a). The angles were determined by the heat flux during the solidification. This was also observed in the corner area of S2 (Fig. 3c).

Equiaxed grains were observed near the bottom of the Y-plane in the overhang, as shown in Fig. 4a and c. During the manufacturing process, the overhang was surrounded by the raw powder. The β phase initially nucleated with random orientation at the first-melt layers, as there was no obvious thermal gradient due to the ineffective heat loss through the metal powder. The conduction of the powder was much lower than the stainless steel base stage. With the increase of the height, the heat loss from the melt pool to the pre-solidified layers became the dominant heat loss path during the solidification. The β phase (cubic crystals) in the chill zone grew dendritically in <100> direction, which was close to the direction of heat flow, and hence they grew fastest and was able to outgrow less favorably oriented neighbors. This led to the formation

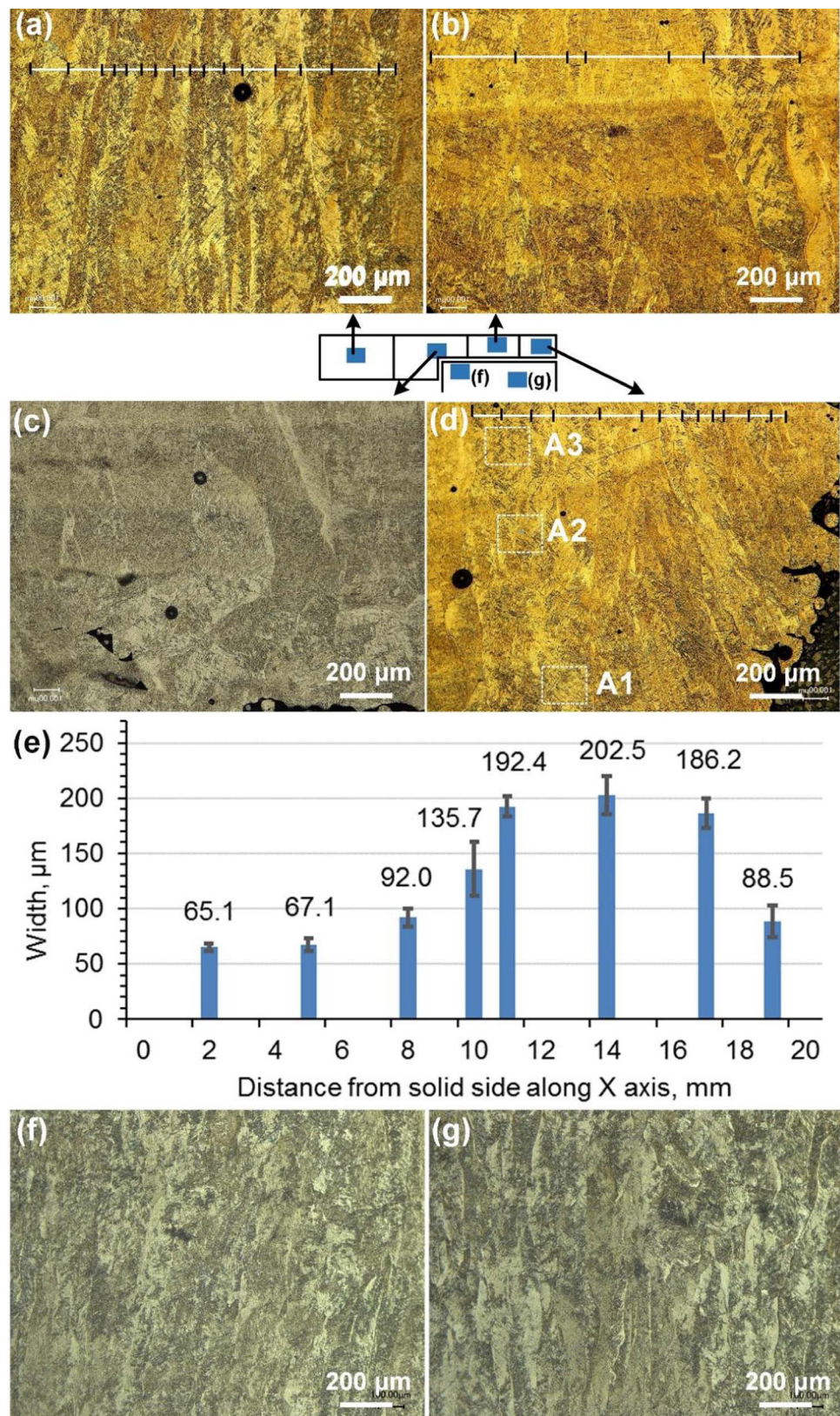


Fig. 5. EBM produced Ti-6Al-4V SG sample: optical microstructure of (a) S1, (b) S3, (c) S2, and (d) S4; (e) width of columnar structures changing along the X-axis at the height close to the top end surface; (f, g) solid part underneath of the overhang; A1, A2, and A3 stands for the bottom, middle, and top regions of the overhang.

of the columnar β phase with $<100>$ almost parallel to the Z-axis. The transition area is shown clearly in Fig. 4c.

The lower cooling rate caused by the ineffective heat loss at the overhang also led to wider columnar structures, as shown in Fig. 4b and

c. This changing trend was observed clearly in the transition region between the solid and the overhang, as shown in Fig. 3d. It is known that a higher cooling rate promotes the formation of smaller columnar β grains because more nuclei can be generated and form finer grains in a

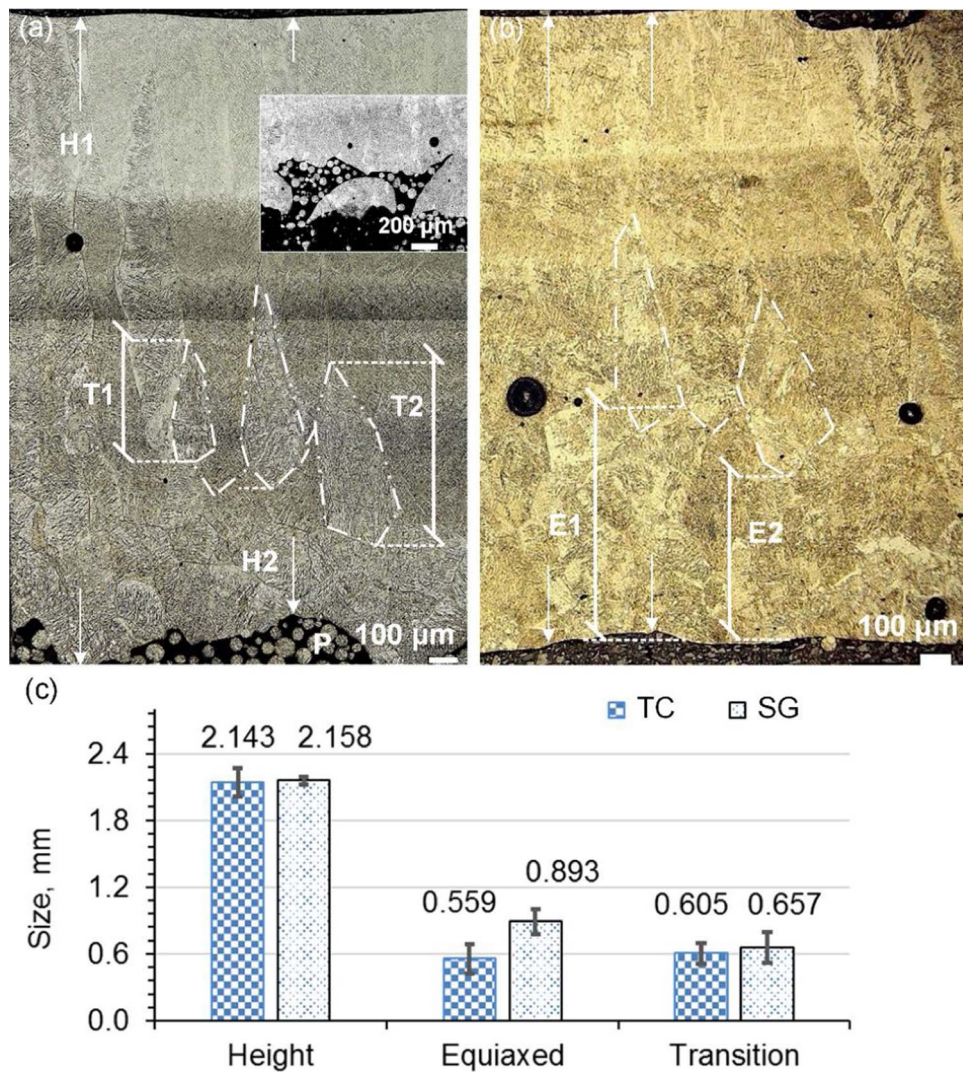


Fig. 6. Compare of the equiaxed grains and the transition zone from equiaxed to columnar grains in (a) TC part (H1/H2: height of the overhang feature, T1/T2: height of the transition zone, P: metal powder) and (b) SG part, (E1/E2: thickness of the equiaxed grains), and (c) the statistical results.

long and narrow columnar morphology (Zhang et al., 2016). The width of the columnar β structure was measured by a statistical method with the measuring example shown in Fig. 4b. According to the statistical values in Fig. 4e, the overhang has a width of 176.3–194.4 μm while the solid has a width of 65.9–70.2 μm , especially the contour scanning region that only shows a width of 46.5 μm . This attributes to the high cooling rate at the contour region, as they were in direct contact with the metal powder. A small fraction of the heat was passed to the metal powder in addition to the previous fabricated solid, and this consequently resulted in a larger cooling rate in the contour scan tracks than the inner hatch scan beads. This was consistent with literature reports that the width of the columnar structure fell in 20–200 μm (Al-Bermani et al., 2010).

The microstructure of SG presents some similar characteristics with the TC part. As shown in Fig. 5, columnar microstructures were revealed in the contour scanned region, which had an angle with the Z-axis that determined by the heat loss through the metal powder and the previously solidified layers. The columnar structure in the middle of the solid region grew along the Z-axis, which presented a narrower width than that in the overhang, as can be seen from Fig. 5a and b. In addition, more defects were revealed around the corner of the interface, including pores and un-melt metal powder.

However, the SG part presents a slow changing trend in the width of the columnar structure, while TC part shows a sharp increase/drop at

the interface from the solid to the overhang and the right end of the overhang. This was mainly caused by the tooth support, which led to a high cooling rate. However, due to the larger distance from the middle of the sample top surface to the top surface of the cuboid-teeth, there is no bigger difference in the width of the columnar structure for the overhang between SG and TC. As shown in Figs. 4e and 5e, the SG part only shows a slight wider columnar structure than the TC part. This indicated a slight lower cooling rate at the centerline along the X-axis, which attributed to the thick loose metal powder underneath of the overhang. It also implied that the solid part beneath the SG overhang did act as a heat sink to enhance heat transfer during the manufacturing process, which increased the thermal gradient at the overhang region. The microstructure in the solid-support part below SG overhang is shown in Fig. 5f and g, which is similar with the microstructure observed in the solid region of the SG part.

Another significant difference between the TC and SG parts was the bottom surface roughness of the overhang. In Fig. 6, the TC part was full of bumps and hollows with un-melt metal powders attached to the bottom surface, while the SG part presented a clean and flat bottom surface. This indicated that sink and dross phenomena occurred during manufacturing of the TC part. As shown in the enlarged area in Fig. 6a, the melted metal is completely separated from the main body. During the manufacturing, the loose metal powder under the overhang could not supply enough support strength for the melted metal, which has a

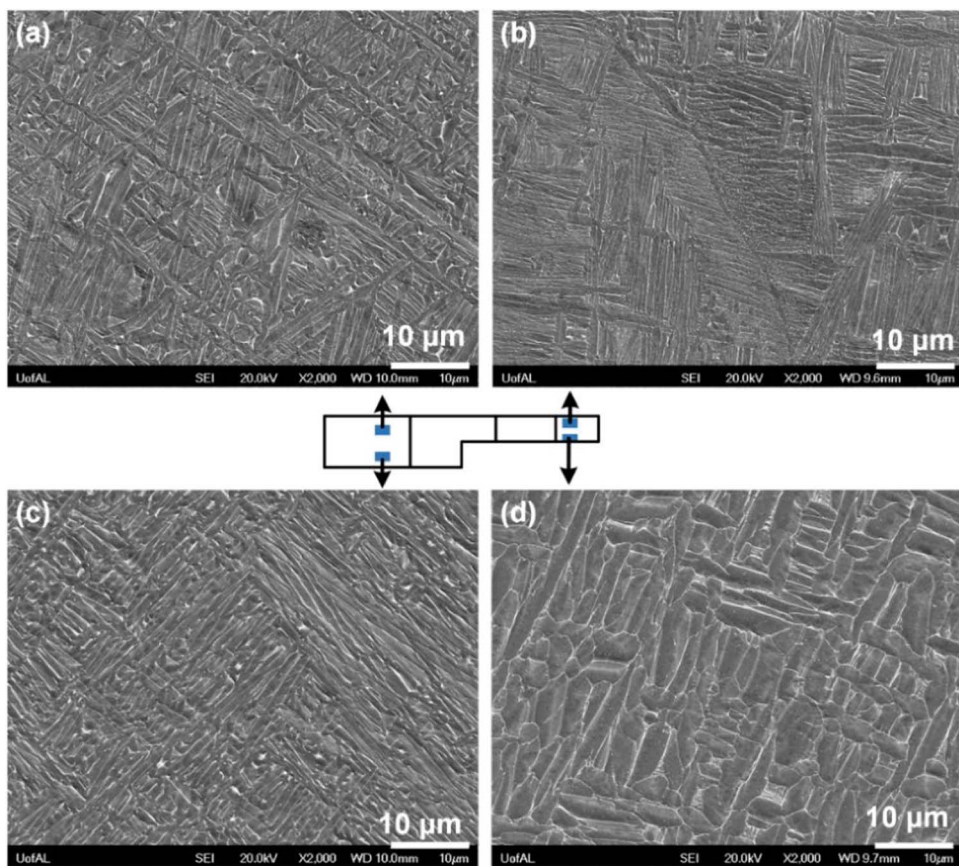


Fig. 7. Microstructures of Ti-6Al-4V alloy from 4 different locations of the TC part.

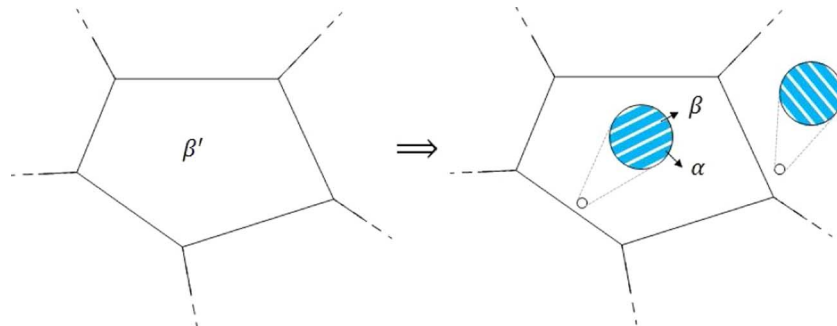


Fig. 8. Schematic illustration of microstructural evolution of EBM-produced Ti-6Al-4V alloy during the phase transformation.

higher density than the loose powder. This led to the occurrence of the roughness of the surface and the sink effects. This comparison stated that the solid part in SG part did supply a good support for the melted metal.

The height of the as-fabricated overhang was measured based on the optical images with the measuring examples shown in Fig. 6a and b. According to the statistic results plotted in Fig. 6c, there is no significant difference in the height of the overhang. However, the TC part presents a much larger standard deviation, which is about 3 times larger than the SG part. In addition, only one or two layers of equiaxed grains were observed at the bottom of the overhang in TC part while three or four layers of equiaxed grains were revealed in the SG part (Fig. 6). The thickness of the equiaxed grains for the TC and SG parts were 0.559 mm and 0.893 mm, respectively. The TC part presented a fast transition from the equiaxed grains to the columnar grains, as indicated by the transition grains highlighted by the dash lines in Fig. 6a and b. These phenomena were caused by the variation of the cooling rate during the manufacturing process. As the boundaries of the

overhang for the TC part were supported by the cuboid-tooth structure, the main heat loss path for the overhang was from the melt pool to the tooth contact support structure. This definitely led to a higher cooling rate and a faster changing rate than that in the SG part, which further resulted in the fast transition from the equiaxed grains to the columnar structure.

3.2. SEM analysis

The SEM morphology of Ti-6Al-4V alloy from S4 of TC part is shown in Fig. 7. Fine Widmanstätten structure ($\alpha + \beta$), was identified inside of equiaxed/columnar grains. However, the bottom area shows a fine fully equiaxed type α/β microstructure (Fig. 7d) while the top area presents a fully lamellar type α/β microstructure (Fig. 7b), which indicates a varied cooling rate in the overhang. During manufacturing, the main heat flux path was from the melt pool to the powder at the initial layers and it gradually changed to the path from the melt pool to the former solidified layers, especially in the overhang region. The thermal history

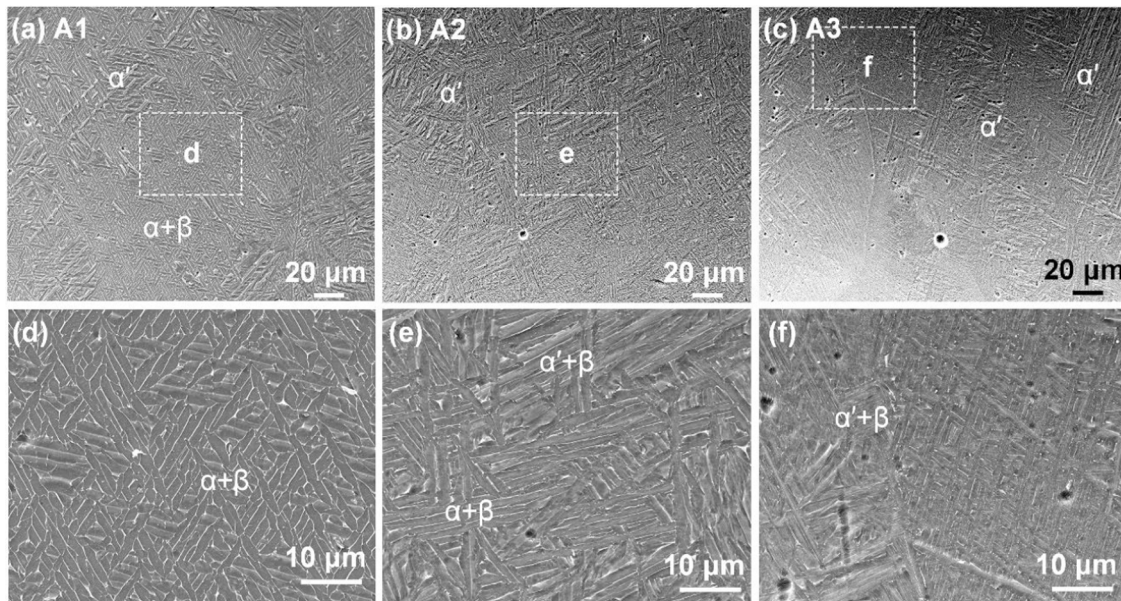


Fig. 9. Microstructure of Ti-6Al-4V SG samples: (a–c) SEM images from the location of A1 (Bottom), A2 (Middle), and A3 (top) in Fig. 5d, respectively; (e–f) SEM images under a higher magnification corresponding to the enclosed region in (a–c), respectively.

significant affected the microstructure evolution (Zaefferer and Wright, 2009). Upon continuous cooling from the β -transus temperature, the initial α -phase nucleates at β -grain boundaries. The cooling rate during the allotropic transformation from the bcc β -phase to the hcp α -phase was the most important parameter controlling the final microstructure. Depending on thermal processing conditions, the α particles develop into equiaxed or acicular lath structures (Tiley et al., 2014). In the columnar/equiaxed β grains, α -phase eventually grew as parallel lamellae with the same crystal orientation within the same β grain until it meets other colonies nucleated at other grain boundaries (Baufeld et al., 2010), as illustrated in Fig. 8. There was no preferred direction for the α -phase within the equiaxed β grains. However, all of the individual α lamellae were separated by a very small amount of β in α boundaries (Tan et al., 2016, 2015a).

In addition, there is a significant changing in the α -lath growing direction. In Fig. 7b, most α laths grew almost parallel to the beam scanning plane. This indicated a higher thermal gradient in the scanning plane due to the heat loss horizontally. Considering the contour-distributed support teeth, it was difficult to understand that the main heat loss path was from the melt pool to the peripheral teeth in addition to the previous solidified solid, which led to this morphology of α laths.

The variation of the thermal process that caused by the changing of the external morphology of the part also had a significant influence on the microstructural evolution during the EBM process. The A1–A3 regions in Fig. 5d under SEM are shown in Fig. 9, which shows clearly that with the increase of the build height, the proportion of the α phase decreased along with the increase of martensitic phase, α' (Tan et al., 2015b). Especially for A3, the region close to the top surface, where the α' in long orthogonally oriented acicular plates were full of the Y-plane (Fig. 9c) (Wang and Wu, 2012). The α' was transformed from the β phase under a very high cooling rate. This also can be seen intuitively in Figs. 4d and 5d, in which the differences between them can be distinguished by the brightness under the optical microscope.

β phase is usually located at the grain boundaries and triple points. Its area fraction was characterized by estimating the fraction of the white area in SEM images using ImageJ. The measuring example is shown in Fig. 10e and the final statistical results are shown in Fig. 10a and c. The area fraction of the β phase in the TC overhang increases from the solid (7.8%) to the overhang (13.9%). For the area in the Y-plane close to the top surface of the sample, the β phase fraction is higher than the area close to the bottom surface, and the overhang

region shows higher statistic values.

Moreover, the variation of the thermal process also affected the characteristic size of the phases. Fig. 10b lists the statistic results of the α -lath width in the samples, which was characterized using SEM images, as shown in Fig. 10f. Based on the quantized values, the width of the α -lath increased from the solid to the overhang. It increased from 0.60 μm to 0.75 μm , and from 0.79 μm to 1.79 μm for the bottom and the top area, respectively. Furthermore, at the location close to the top surface, the α -lath has a higher value than the location close to the bottom surface of the overhang, as clearly shown in Fig. 10b.

The SG part also presents a similar changing trend with the β phase, as shown in Fig. 10d. One of the significant difference in β fraction is that SG part has higher values than the TC part at the area close to the top surface. This is because α' phases are also included in the statistic results as the α' phase also has a shallow white color. The SG part has a finer α -lath in overhang than the TC part. This is because the solid part underneath of the SG overhang part acted as a heat sink to enhance heat transfer, which led to a higher thermal gradient and further led to a coarser α lath. However, the tip end of the overhang in TC shows a much finer α lath than the SG part, which is attributed to the higher thermal gradient resulted from the tooth support at the contour area.

3.3. Defects analysis

Defects, such as unmelt powder and pores, were observed in the samples. First, S4 of SG part had a curved bottom surface. This was caused by the compressive residual stress in the Y-plane of the as-deposited parts (Yadroitsava and Yadroitsev, 2015), which led to the tip of the part curved toward the positive Z-axis. Second, unmelt powder (Gong et al., 2015) and pores (Wang and Beese, 2017) were observed in the part, as shown in Fig. 11a, in which area A1 stands for the big spherical pores and A2 represents the irregular pores. The spherical pores are mainly from the gas entrapped inside the powder particles during the powder atomization process (Wang et al., 2017) and the irregular pores come from lack of fusion defects (DebRoy et al., 2018). In Fig. 11c, the irregular pores are accompanied by un-melted particles and unconsolidated materials. Pores are noticeable in all the four specimens from SG part. The statistical data collected are plotted in Fig. 11b, which indicates that the overhang has a higher porosity and defects than the solid. This mainly resulted from the inadequate support of the overhang region, which prompted the occurrence of sink, dross,

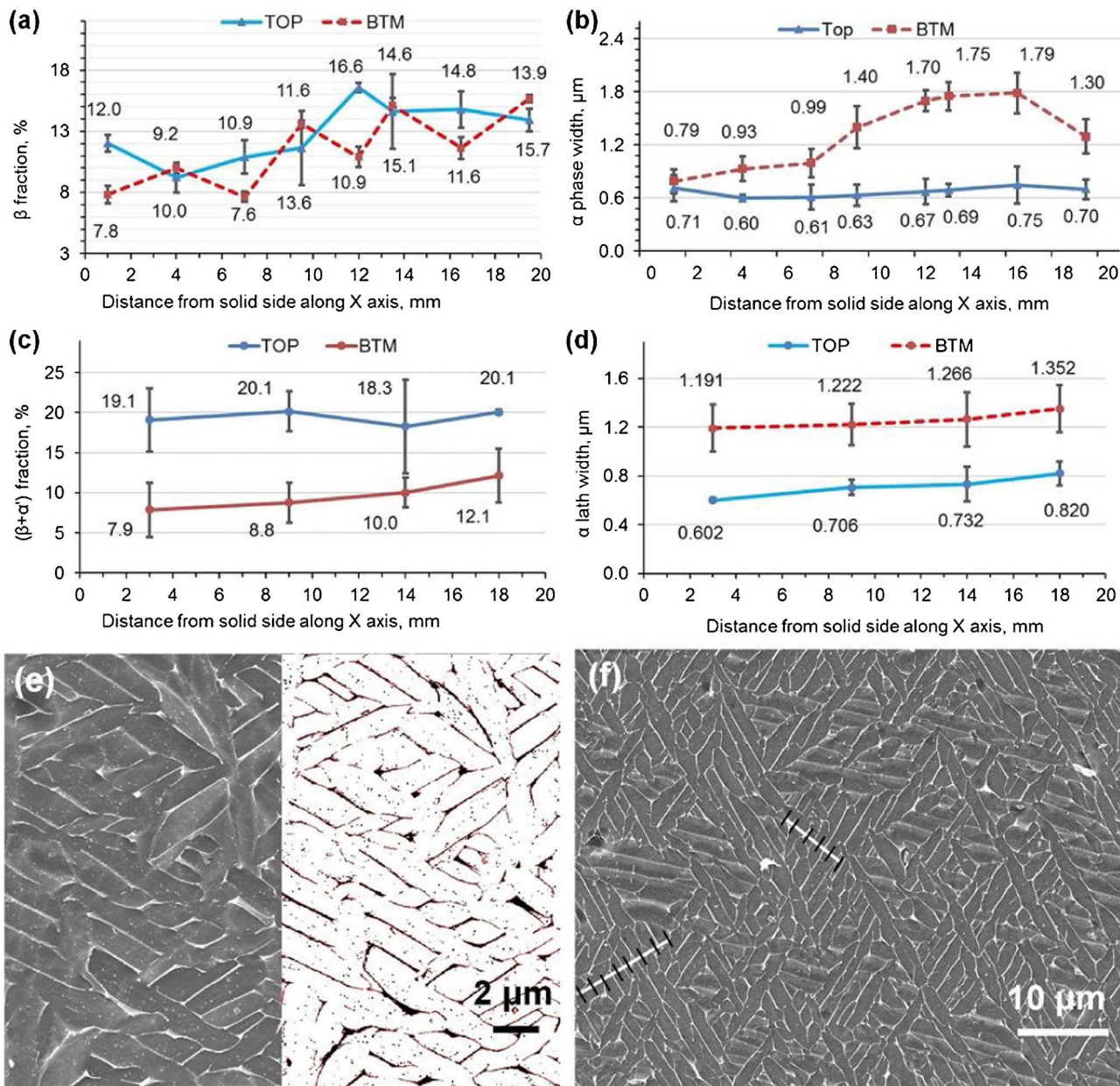


Fig. 10. Statistic results of β fraction: (a) TC sample and (c) SG sample; Statistic results of α -lath width: (b) TC sample and (d) SG sample; (e) example illustrating the measurement of β fraction and (f) example of the measuring the width of α -lath.

warping. This was much more serious in the overhang of TC part, as shown in Fig. 4, which has a higher porosity than the SG part (Fig. 5).

Fig. 11c illustrates the defects at the corner of the overhang part. There were two big holes with a length of about $500\text{ }\mu\text{m}$. In some holes, there were some un-melted particles accompanied with segregation. In addition, there was a white area with a crack at the center of it. Through EDX analysis of this region, it revealed the presence of Cr, Fe, and Ni that all acted to stabilize the β phase, as shown in Table 1. For the region of P4, which filled around the unmelt powder, it was segregation as it had a higher content of oxygen.

3.4. Texture analysis

Columnar and equiaxed microstructures in SG part are revealed clearly in the orientation maps shown in Fig. 12a–e. The boundaries of the β' are marked with white lines in the image quality (IQ) map (Fig. 12f). The relatively poor quality was observed in some regions in IQ map, which was caused by the higher internal strains (Kelly, 2004).

Narrower columnar structures were observed in the wider columnar structure, as marked by the thin white lines in Fig. 12f, and the α phase within them almost shares the same orientation.

During the phase transformation, the prior directional solidified β phase transferred into α/α' phase following the Burgers relationship, $\{0001\}\alpha \parallel \{110\}\beta$ (parallel planes), and $\langle 1120 \rangle \alpha \parallel \langle 111 \rangle \beta$ (parallel directions). Correspondingly, the texture in β' phase was transmitted to a texture in the α/α' phase, as shown in the $\langle 11\bar{2}0 \rangle \alpha$ pole figure, Fig. 12i–k, where the $\langle 11\bar{2}0 \rangle \alpha$ pole figure looks similar to $\langle 110 \rangle \beta$ pole figure (Baufeld et al., 2010). In Fig. 12i, α phase has a strong $\langle 0001 \rangle$ texture parallel to the z-axis. However, the texture intensities of the α phase are much lower than those of the β' phase. This attributes to the 12 distinct variants of α orientations which can be formed from one parent β grain due to the crystal symmetry. In addition, the variant selection was observed in the samples (Antonyamy et al., 2013) that α grains within one β' grain tend to group together their variants, as can be seen in Fig. 12a–e. This leads to the relatively strong texture in α phase.

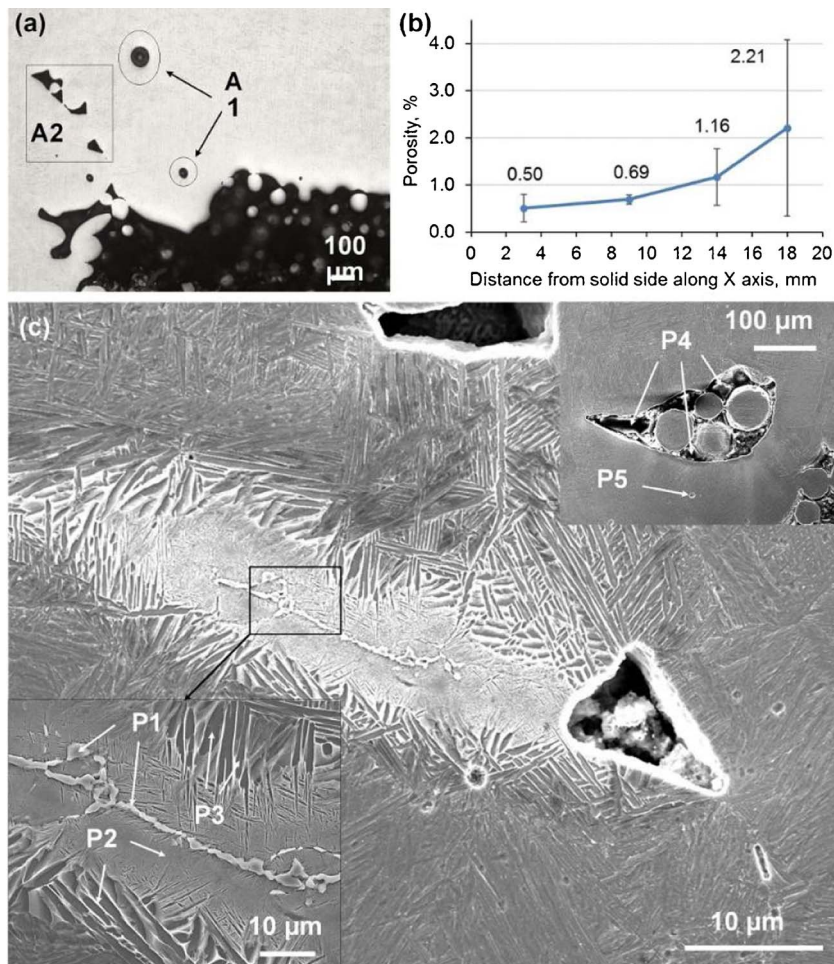


Fig. 11. Y-plane of the SG samples: (a) A1, spherical pores and A2, irregular pores, (b) statistic results of the porosity, and (c) defects under SEM.

Table 1
EDS analysis results at the locations P1–P5 in Fig. 11(c).

(d) Precipitates	Powder	P1 Carbide	P2 β + Carbide	P3 α phase	P4 Carbide	P5 β phase (V)
Composition (Wt%)						
Ti	90.0	57.9	68.6	89.6	23.1	91.0
Al	6.0	2.5	4.3	5.5	0.8	1.8
V	4.0	0.9	6.1	3.3	1.8	6.6
Fe	< = 0.25	4.8	2.0	0.2	1.9	0.5
O	< = 0.2	2.6	8.3	0.9	30.2	
Ni		25.0	6.3	0.8		
Si		0.2		1.4		
F		4.7	4.3	3.2		
Cr		1.5	0.7			
Na				8.7		

The EBSD pole figures for the β phase show a strong texture (Fig. 12). The β phase in Fig. 12a presents a strong intensity with its max value around 25 (Fig. 12i), which is similar to rolled sheet counterparts. From the solid to the overhang, the intensity of the β phase first slightly decreased and then increased at the end (Fig. 12i–k). There was also a sharp increase in the maximum intensity of the texture at the bottom region. This was caused by the narrower columnar structures at the tip of the overhang, which presented strong textures with higher intensities in both β phase and α phase, as displayed in Fig. 12c. For the overhang, the bottom equiaxed grains have a relatively weak texture

than the top columnar grains.

3.5. Microhardness

The Vickers hardness of the TC and SG parts changing along the distance from the left solid along the x-axis were plotted in Fig. 13. Generally, the solid of the part shows a slightly higher average value (3.41/3.67 GPa) than the overhang (3.29/3.66 GPa), which results from the differences in the microstructure size. As mentioned above, both the width of prior β structure and α lath have a larger size at the overhang than the solid. At the right end of the overhang, the TC part shows a slightly increasing trend while the SG part presents a continued decreasing trend, which has the same changing trend in the width of α -lath (Fig. 10) that resulted from the different support structures. The SG part also presents higher hardness values than the TC part (Fig. 13), which is a combined effect of the difference in phase fraction and the grain size. As mentioned above, the SG part has a higher fraction of α' phase and finer microstructure, which leads to the higher microhardness values. The average values are in the range of 3.16 GPa–3.50 GPa for the TC part and 3.58 GPa–3.78 GPa for the SG part.

3.6. Residual stresses

The average value of the residual stress at the centerline of the TC and SG parts changing along the X-axis are plotted in Fig. 14. In general, the EBM fabricated parts have a compressive residual stress randomly distributed in the Y-plane along the center line. As shown in Fig. 14a, the TC part has a compressive residual stress with some

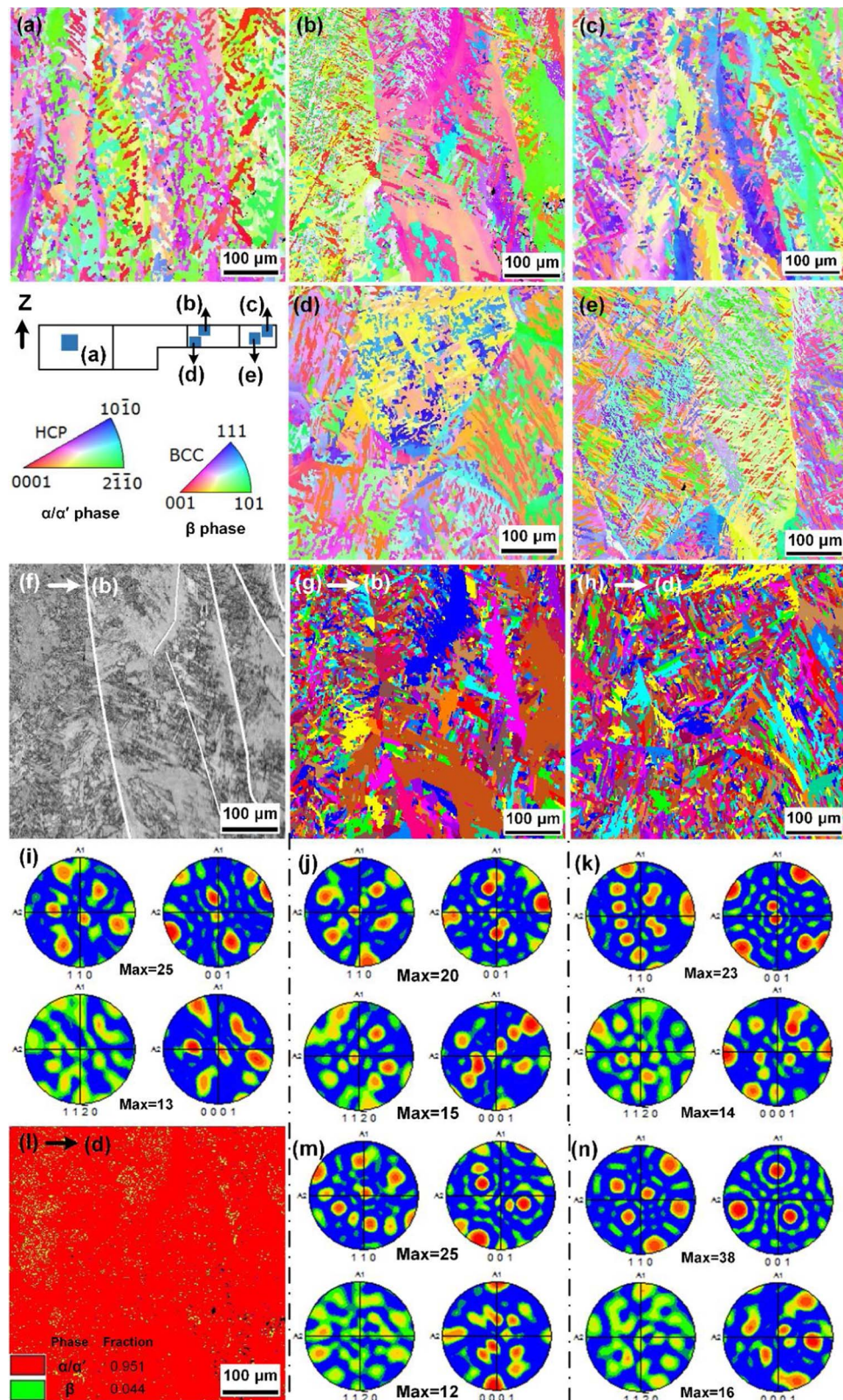


Fig. 12. Ti-6Al-4V SG part: (a–e) orientation maps of α/α' phase; (f) image quality map of (b); (g, h) grain maps for (b, d); (i–k, m–n) pole figures of α/α' phase corresponding to (a–e), and (l) the phase map corresponding to (d).

locations presenting tensile residual stress at the X-axis of 16–17 mm. The maximum absolute value of the residual stress is 271 MPa, which is 31.6% of its yield strength (858 MPa) (Roy, 2013). The average value of the compressive residual stress for the TC part is 200 MPa in the solid and 77 MPa in the overhang. This resulted from the lower temperature

gradient during the manufacturing process. However, there is no significant change in the absolute values of the residual stress for the SG part, as shown in Fig. 14b, which also indicated that the solid part beneath the overhang did increase the thermal gradient during the manufacturing process. On the other hand, the larger residual stress led

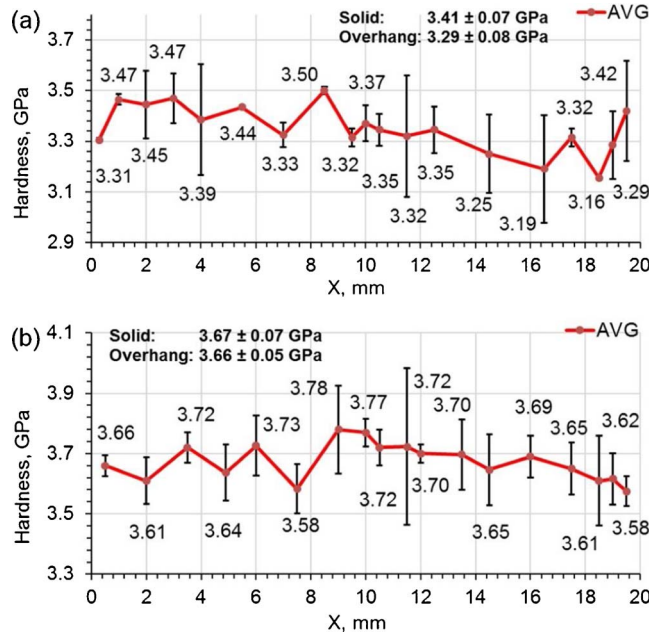


Fig. 13. Average Vickers Hardness, H_V (1kgf), of EBM Ti-6Al-4V parts changing with the distance from the solid side along the X axis: (a) TC part and (b) SG part.

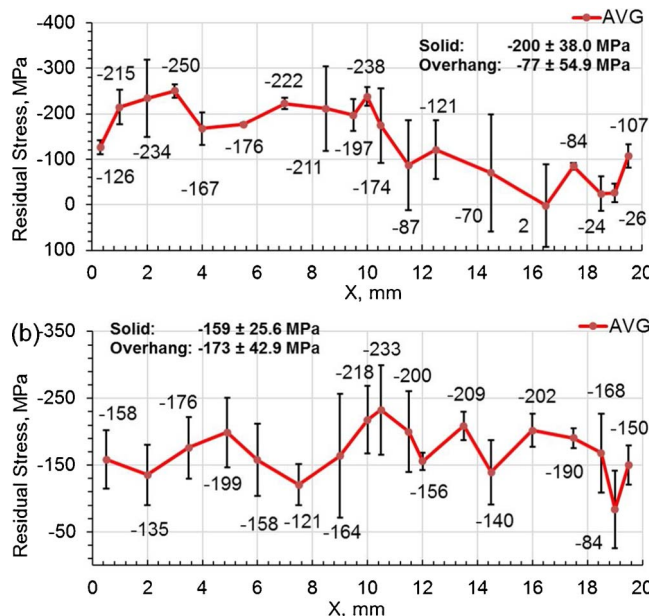


Fig. 14. Residual stress of EBM Ti-6Al-4V parts at different locations changing along with the distance from the solid side along the X-axis: (a) TC part and (b) SG part.

to the warping of the overhang sample at the tip of the S4, as can be seen in Fig. 14d, as there are no constraints at the right terminal of the SG overhang.

In addition, there was a sharp increase in the absolute residual stress at the transition region. The average compressive residual stress in the TC part increased from 197 MPa to 238 MPa and then decreased to 87 MPa. This was even more obvious in the SG part as the residual stress increased from (164 MPa) to the overhang (233 MPa) and then decreased to 156 MPa. This was brought about by the changing of the macroscopic geometry from the solid to the overhang, where formed a right angle interface between them. This caused the stress concentration at the corner, the same finding was obtained in a simulation study (Bobbio et al., 2017).

Moreover, compared to the SG part, the TC part showed a larger

increase in compressive residual stress at the right end of overhang, especially the bottom region. This was caused by the higher temperature gradient at the right end of the TC part as the heat passed away through the cuboid-tooth support. Based on the changing trends of the residual stress and the hardness, the residual stress did not show remarkable effects on the hardness of the Ti-6Al-4V part.

3.7. Comparison of TC and SG designs

Based on the former analysis, the solid part in the SG support design did work as a heat sink to enhance heat dissipation during the manufacturing process, which altered the thermal characteristics of the process and consequently the overhang microstructures, and further improved mechanical performance of the overhang. However, the SG part warped at the end-tip of the overhang, which was much more serious than the TC part. Comprehensive analysis of the two designs, SG support with teeth at the tip-end is recommended, which takes advantages of the two designs. To get a better support design in practical application, the parameters related this new design will be optimized in following studies, such as the solid gap amount, the number of teeth in TG, and the size of the teeth.

4. Conclusions

Two Ti-6Al-4V parts with different support structures (solid-gap vs. thin-wall tooth contact) were fabricated by the powder bed fusion electron beam additive manufacturing technology. The effects of the support structures on the microstructures and mechanical properties of the as-built parts were investigated. Based on the experimental results, the major findings are summarized as follows.

- The Y-plane had a typical β columnar structure with fine ($\alpha + \beta$) within it. Martensitic phase, α' , was also observed in the specimens with its content increased from the bottom to the top of the part.
- The equiaxed microstructures were observed at the location near the bottom surface of the overhang and gradually grew into wider columnar structures, around 176.3–202.5 μm , in contrast to about 65.9–70.2 μm in the solid. The width of the α -lath increased from the solid (0.60 μm –0.75 μm) to the overhang (0.79 μm to 1.79 μm).
- The overhang presented more defects, including porosity and unmelted particles, compared to the solid region. The largest pores, with a diameter of about 500 μm , were observed at the interface of the solid and the overhang.
- There was a strong texture in the β' phase, and the texture transferred to the texture of α/α' phase during the phase transformation.
- The solid region had a higher hardness than the overhang due to the composition of the phases and the size of the microstructure. The Vickers hardness of the SG part was in the range of 3.58–3.78 GPa while the Vickers hardness for the TC part was in the range of 3.16–3.50 GPa. This was caused by the lower fraction of α' phase and coarser microstructure in the TC part.
- Compressive residual stresses were revealed in the Ti-6Al-4V samples with some locations showing minor tensile residual stresses. The maximum absolute value was 271 MPa, which was 31.6% of its yield strength. There was a sharp increase in the average residual stress magnitude at the interface corner between the solid and the overhang due to the occurrence of the stress concentration at the corner resulted from the geometry change.
- The solid part beneath the overhang of the SG part functioned as a heat sink to enhance heat dissipation during the manufacturing process, which improved the microstructures and mechanical properties in the overhang. However, a serious warping was observed at the overhang of the SG part. Comprehensive consideration of the two designs, SG with teeth at the tip-end of the support is recommended. The gap between the solid part and the overhang will also need to be optimized.

Acknowledgements

This work was supported by NSF1335481/1739435. Marshall Space Flight Center fabricated experimental samples.

References

- Al-Bermani, S.S., Blackmore, M.L., Zhang, W., Todd, I., 2010. The origin of microstructural diversity, texture, and mechanical properties in electron beam melted Ti-6Al-4V. *Metall. Mater. Trans. A* 41, 3422–3434. <http://dx.doi.org/10.1007/s11661-010-0397-x>.
- Antonyamy, A.A., Meyer, J., Prangnell, P.B., 2013. Effect of build geometry on the β -grain structure and texture in additive manufacture of Ti6Al4V by selective electron beam melting. *Mater. Charact.* 84, 153–168. <http://dx.doi.org/10.1016/j.matchar.2013.07.012>.
- Arcam, 2018a. Arcam Brochure [WWW Document]. (Accessed 1 January 2018). <http://www.arcam.com/wp-content/uploads/arcamebm-corp-brochure-fnlv3.pdf>.
- Arcam, 2018b. Ti6Al4V Titanium Alloy [WWW Document]. Arcam EBM Syst. <http://www.arcam.com/wp-content/uploads/Arcam-Ti6Al4V-Titanium-Alloy.pdf>.
- Baufeld, B., Van Der Biest, O., Dillien, S., 2010. Texture and crystal orientation in Ti-6Al-4V builds fabricated by shaped metal deposition. *Metall. Mater. Trans. A Phys. Metall. Mater. Sci.* 41, 1917–1927. <http://dx.doi.org/10.1007/s11661-010-0255-x>.
- Bobbio, L.D., Qin, S., Dunbar, A., Michaleris, P., Beese, A.M., 2017. Characterization of the strength of support structures used in powder bed fusion additive manufacturing of Ti-6Al-4V. *Addit. Manuf.* 14, 60–68. <http://dx.doi.org/10.1016/j.addma.2017.01.002>.
- Calignano, F., 2014. Design optimization of supports for overhanging structures in aluminum and titanium alloys by selective laser melting. *Mater. Des.* 64, 203–213. <http://dx.doi.org/10.1016/j.matdes.2014.07.043>.
- Carlsson, S., Larsson, P.-L., 2001. On the determination of residual stress and strain fields by sharp indentation testing.: Part II: experimental investigation. *Acta Mater.* 49, 2193–2203. [http://dx.doi.org/10.1016/S1359-6454\(01\)00123-9](http://dx.doi.org/10.1016/S1359-6454(01)00123-9).
- Chivel, Y., Smurov, I., 2011. Temperature monitoring and overhang layers problem. *Phys. Procedia* 12, 691–696. <http://dx.doi.org/10.1016/j.phpro.2011.03.086>.
- de Formanoir, C., Michotte, S., Rigo, O., Germain, L., Godet, S., 2016. Electron beam melted Ti-6Al-4V: microstructure, texture and mechanical behavior of the as-built and heat-treated material. *Mater. Sci. Eng. A* 652, 105–119. <http://dx.doi.org/10.1016/j.msea.2015.11.052>.
- DebRoy, T., Wei, H.L., Zuback, J.S., Mukherjee, T., Elmer, J.W., Milewski, J.O., Beese, A.M., Wilson-Heid, A., De, A., Zhang, W., 2018. Additive manufacturing of metallic components – process, structure and properties. *Prog. Mater. Sci.* 92, 112–224. <http://dx.doi.org/10.1016/j.pmatsci.2017.10.001>.
- Ding, Y., Akbari, M., Kovacevic, R., 2017a. Process planning for laser wire-feed metal additive manufacturing system. *Int. J. Adv. Manuf. Technol.* 1–11. <http://dx.doi.org/10.1007/s00170-017-1179-z>.
- Ding, Y., Dwivedi, R., Kovacevic, R., 2017b. Process planning for 8-axis robotized laser-based direct metal deposition system: a case on building revolved part. *Robot. Comput. Integrat. Manuf.* 44, 67–76. <http://dx.doi.org/10.1016/j.rcim.2016.08.008>.
- Ding, Y., Kovacevic, R., 2016. Feasibility study on 3-D printing of metallic structural materials with robotized laser-based metal additive manufacturing. *JOM* 68, 1774–1779. <http://dx.doi.org/10.1007/s11837-016-1929-7>.
- Ding, Y., Warton, J., Kovacevic, R., 2016. Development of sensing and control system for robotized laser-based direct metal addition system. *Addit. Manuf.* 10, 24–35. <http://dx.doi.org/10.1016/j.addma.2016.01.002>.
- Eylon, D., Seagle, S.R., 2001. Titanium technology in the USA—an overview. *J. Mater. Sci. Technol.* 17, 439–443.
- Facchini, L., Magalini, E., Robotti, P., Molinari, A., 2009. Microstructure and mechanical properties of Ti-6Al-4V produced by electron beam melting of pre-alloyed powders. *Rapid Prototyp. J.* 15, 171–178.
- Gan, M.X., Wong, C.H., 2016. Practical support structures for selective laser melting. *J. Mater. Process. Technol.* 238, 474–484. <http://dx.doi.org/10.1016/j.jmatprotc.2016.08.006>.
- Gong, H., Rafi, K., Gu, H., Janaki Ram, G.D., Starr, T., Stucker, B., 2015. Influence of defects on mechanical properties of Ti-6Al-4 V components produced by selective laser melting and electron beam melting. *Mater. Des.* 86, 545–554. <http://dx.doi.org/10.1016/j.matdes.2015.07.147>.
- Gong, X., Lydon, J., Cooper, K., Chou, K., 2014. Beam speed effects on Ti-6Al-4V microstructures in electron beam additive manufacturing. *J. Mater. Res.* 29, 1951–1959.
- Hrabe, N., Quinn, T., 2013. Effects of processing on microstructure and mechanical properties of a titanium alloy (Ti-6Al-4V) fabricated using electron beam melting (EBM), part 2: energy input, orientation, and location. *Mater. Sci. Eng. A* 573, 271–277. <http://dx.doi.org/10.1016/j.msea.2013.02.065>.
- Hu, H.J., Ying, Y.L., Ou, Z.W., Wang, X.Q., 2017. Comparisons of microstructures and texture and mechanical properties of magnesium alloy fabricated by compound extrusion and direct extrusion. *Mater. Sci. Eng. A* 695, 360–366. <http://dx.doi.org/10.1016/j.jmatprotc.2017.03.103>.
- Jamshidinia, M., Wang, L., Tong, W., Kovacevic, R., 2014. The bio-compatible dental implant designed by using non-stochastic porosity produced by Electron Beam Melting (EBM). *J. Mater. Process. Technol.* 214, 1728–1739. <http://dx.doi.org/10.1016/j.jmatprotc.2014.02.025>.
- Järvinen, J.-P., Matilainen, V., Li, X., Piili, H., Salminen, A., Mäkelä, I., Nyrhilä, O., 2014. Characterization of effect of support structures in laser additive manufacturing of stainless steel. *Phys. Procedia* 56, 72–81. <http://dx.doi.org/10.1016/j.phpro.2014.08.099>.
- Jhabvala, J., Boillat, E., André, C., Glardon, R., 2012. An innovative method to build support structures with a pulsed laser in the selective laser melting process. *Int. J. Adv. Manuf. Technol.* 59, 137–142. <http://dx.doi.org/10.1007/s00170-011-3470-8>.
- Kelly, S.M., 2004. Thermal and Microstructure Modeling of Metal Deposition Processes With Application to Ti-6Al-4V.
- Kruth, J.-P., Mercelis, P., Van Vaerenbergh, J., Craeghs, T., 2007. Feedback control of selective laser melting. Proceedings of the 3rd International Conference on Advanced Research in Virtual and Rapid Prototyping. pp. 521–527.
- Langelaar, M., 2016. Topology optimization of 3D self-supporting structures for additive manufacturing. *Addit. Manuf.* 12 (Part A), 60–70. <http://dx.doi.org/10.1016/j.addma.2016.06.010>.
- Lu, S.L., Qian, M., Tang, H.P., Yan, M., Wang, J., StJohn, D.H., 2016. Massive transformation in Ti-6Al-4V additively manufactured by selective electron beam melting. *Acta Mater.* 104, 303–311. <http://dx.doi.org/10.1016/j.actamat.2015.11.011>.
- Murr, L., Gaytan, S., Medina, F., Martinez, E., Hernandez, D., Martinez, L., Lopez, M., Wicker, R., Collins, S., Arcam, A.B., 2009. Effect of build parameters and build geometries on residual microstructures and mechanical properties of Ti-6Al-4V components built by electron beam melting (EBM). In: 20th Solid Freeform Fabrication Symposium. Austin, TX, pp. 3–5 August.
- Poyraz, Ö., Yasa, E., Akbulut, G., Orhangil, A., Pilat, S., 2015. Investigation of support structures for direct metal laser sintering (DMLS) of in625 parts. *Solid Freeform Fabrication Symposium*. pp. 560–574.
- Roy, L., 2013. Variation in Mechanical Behavior Due to Different Build Directions of ti6al4v Fabricated by Electron Beam Additive Manufacturing Technology. *Dep. Mech. Eng. The University of Alabama, TUSCALOOSA, Alabama*.
- Song, B., Dong, S., Liu, Q., Liao, H., Coddet, C., 2014. Vacuum heat treatment of iron parts produced by selective laser melting: microstructure, residual stress and tensile behavior. *Mater. Des.* 54, 727–733. <http://dx.doi.org/10.1016/j.matedes.2013.08.085>.
- Strano, G., Hao, L., Everson, R.M., Evans, K.E., 2013. A new approach to the design and optimisation of support structures in additive manufacturing. *Int. J. Adv. Manuf. Technol.* 66, 1247–1254. <http://dx.doi.org/10.1007/s00170-012-4403-x>.
- Tan, X., Kok, Y., Tan, Y.J., Desclois, M., Mangelinck, D., Tor, S.B., Leong, K.F., Chua, C.K., 2015a. Graded microstructure and mechanical properties of additive manufactured Ti-6Al-4V via electron beam melting. *Acta Mater.* 97, 1–16. <http://dx.doi.org/10.1016/j.actamat.2015.06.036>.
- Tan, X., Kok, Y., Tan, Y.J., Vastola, G., Pei, Q.X., Zhang, G., Zhang, Y.-W., Tor, S.B., Leong, K.F., Chua, C.K., 2015b. An experimental and simulation study on build thickness dependent microstructure for electron beam melted Ti-6Al-4V. *J. Alloys Compd.* 646, 303–309. <http://dx.doi.org/10.1016/j.jallcom.2015.05.178>.
- Tan, X., Kok, Y., Toh, W.Q., Tan, Y.J., Desclois, M., Mangelinck, D., Tor, S.B., Leong, K.F., Chua, C.K., 2016. Revealing martensitic transformation and α/β interface evolution in electron beam melting three-dimensional-printed Ti-6Al-4V. *Sci. Rep.* 6.
- Thomas, D., Bibb, R., 2008. Identifying the geometric constraints and process specific challenges of selective laser melting. In: Proceedings of Time Compression Technologies Rapid Manufacturing Conference. Coventry, United Kingdom.
- Tiley, J.S., Shiveley, A.R., Pilchak, A.L., Shade, P.A., Groeber, M.A., 2014. 3D reconstruction of prior β grains in friction stir-processed Ti-6Al-4V. *J. Microsc.* 255, 71–77. <http://dx.doi.org/10.1111/jmi.12137>.
- Toh, W., Wang, P., Tan, X., Nai, M., Liu, E., Tor, S., 2016. Microstructure and wear properties of electron beam melted Ti-6Al-4V parts: a comparison study against as-cast form. *Metals (Basel)* 6, 284. <http://dx.doi.org/10.3390/met6110284>.
- Vandenbroucke, B., Kruth, J.-P., 2007. Selective laser melting of biocompatible metals for rapid manufacturing of medical parts. *Rapid Prototyp. J.* 13, 196–203.
- Wang, S., Wu, X., 2012. Investigation on the microstructure and mechanical properties of Ti-6Al-4V alloy joints with electron beam welding. *Mater. Des.* 36, 663–670. <http://dx.doi.org/10.1016/j.matedes.2011.11.068>.
- Wang, X., Chou, K., 2017a. Effects of thermal cycles on the microstructure evolution of Inconel 718 during selective laser melting process. *Addit. Manuf.* 18, 1–14. <http://dx.doi.org/10.1016/j.addma.2017.08.016>.
- Wang, X., Chou, K., 2017b. Electron backscatter diffraction analysis of Inconel 718 parts fabricated by selective laser melting additive manufacturing. *JOM* 69, 402–408. <http://dx.doi.org/10.1007/s11837-016-2198-1>.
- Wang, X., Chou, K., 2015. A method to estimate residual stress in metal parts made by selective laser melting. *Proc. ASME 2015 International Mechanical Engineering Congress and Exposition. American Society of Mechanical Engineers. p. V02AT02A002*.
- Wang, X., Gong, X., Chou, K., 2017. Review on powder-bed laser additive manufacturing of Inconel 718 parts. *Proc. Inst. Mech. Eng. Part B J. Eng. Manuf.* 231, 1890–1903. <http://dx.doi.org/10.1177/0954405415619883>.
- Wang, X., Gong, X., Chou, K., 2015. Scanning speed effect on mechanical properties of Ti-6Al-4V alloy processed by electron beam additive manufacturing. *Procedia Manuf.* 1, 287–295. <http://dx.doi.org/10.1016/j.promfg.2015.09.026>.
- Wang, X., Keya, T., Chou, K., 2016c. Build height effect on the Inconel 718 parts fabricated by selective laser melting. *Procedia Manuf.* 5, 1006–1017. <http://dx.doi.org/10.1016/j.promfg.2016.08.089>.
- Wang, Z., Beese, A.M., 2017. Effect of chemistry on martensitic phase transformation kinetics and resulting properties of additively manufactured stainless steel. *Acta Mater.* 131, 410–422. <http://dx.doi.org/10.1016/j.actamat.2017.04.022>.
- Wang, Z., Palmer, T.A., Beese, A.M., 2016a. Effect of processing parameters on microstructure and tensile properties of austenitic stainless steel 304L made by directed energy deposition additive manufacturing. *Acta Mater.* 110, 226–235. <http://dx.doi.org/10.1016/j.actamat.2016.03.019>.
- Wang, Z., Stoica, A.D., Ma, D., Beese, A.M., 2016b. Diffraction and single-crystal elastic constants of Inconel 625 at room and elevated temperatures determined by neutron diffraction. *Mater. Sci. Eng. A* 674, 406–412. <http://dx.doi.org/10.1016/j.msea.2016.08.010>.

Yadroitsava, I., Yadroitsev, I., 2015. Residual stress in metal specimens produced by direct metal laser sintering. In: International Solid Freeform Fabrication Symposium. Austin, Texas, USA. pp. 614–625.

Zaefferer, S., Wright, S.I., 2009. Electron Backscatter Diffraction in Materials Science. Springer<http://dx.doi.org/10.1007/978-0-387-88136-2>.

Zeng, K., 2015. Optimization of Support Structures for Selective Laser Melting.

Zhang, Z., Farahmand, P., Kovacevic, R., 2016. Laser cladding of 420 stainless steel with molybdenum on mild steel A36 by a high power direct diode laser. Mater. Des. 109, 686–699. <http://dx.doi.org/10.1016/j.matdes.2016.07.114>.